JOURNAL OF APPLIED PHYSICS 116, 103305 (2014)

Spatial profiles of electron and metastable atom densities in positive polarity fast ionization waves sustained in helium

Brandon R. Weatherford,[1,a),b)] Zhongmin Xiong,[2,a),c)] E. V. Barnat,[1,a)] and Mark J. Kushner[2,a)]
[1]*Sandia National Laboratories, Albuquerque, New Mexico 87185-1423, USA*
[2]*Department of Electrical Engineering and Computer Science, University of Michigan, Ann Arbor, Michigan 48109-2122, USA.*

(Received 6 June 2014; accepted 30 August 2014; published online 11 September 2014)

Fast ionization waves (FIWs), often generated with high voltage pulses over nanosecond timescales, are able to produce large volumes of ions and excited states at moderate pressures. The mechanisms of FIW propagation were experimentally and computationally investigated to provide insights into the manner in which these large volumes are excited. The two-dimensional structure of electron and metastable densities produced by short-pulse FIWs sustained in helium were measured using laser-induced fluorescence and laser collision-induced fluorescence diagnostics for times of 100–120 ns after the pulse, as the pressure was varied from 1 to 20 Torr. A trend of center-peaked to volume-filling to wall-peaked electron density profiles was observed as the pressure was increased. Instantaneous FIW velocities, obtained from plasma-induced emission, ranged from 0.1 to 3×10^9 cm s^{-1}, depending on distance from the high voltage electrode and pressure. Predictions from two-dimensional modeling of the propagation of a single FIW correlated well with the experimental trends in electron density profiles and wave velocity. Results from the model show that the maximum ionization rate occurs in the wavefront, and the discharge continues to propagate forward after the removal of high voltage from the powered electrode due to the potential energy stored in the space charge. As the pressure is varied, the radial distribution of the ionization rate is shaped by changes in the electron mean free path, and subsequent localized electric field enhancement at the walls or on the centerline of the discharge.
[http://dx.doi.org/10.1063/1.4895482]

I. INTRODUCTION

In recent years, there has been significant interest in fast ionization wave (FIW) discharges.[1–4] FIWs are generated by the application of nanosecond-duration high voltage pulses, which substantially exceed the threshold for breakdown under quasi-continuous conditions. This overvoltage produces highly non-equilibrium ionization rates, which in turn enable the FIW to propagate over large distances on shorter timescales than those in which instabilities can typically develop.[1] This allows for the production of diffuse, large-volume, uniform discharges at higher pressures than what is typical in direct-current glow discharges.[5] The large population of high energy electrons in the FIW wavefront can, in some cases, efficiently drive inelastic processes without significant heating of the gas.[6]

In one configuration, a FIW discharge can be established within a cylindrical dielectric tube, surrounded by a conductive shield. At one end of the tube is a high voltage electrode, and at the other end is a ground electrode in contact with the shield. In experiments with both positive and negative-polarity high voltage pulses; the wavefront begins at the high voltage electrode and propagates toward the grounded electrode.[7,8] The properties of the ionization wave are determined by several factors, including the geometry of the discharge tube and electrodes, gas pressure, and the polarity and shape of the voltage waveform.[7] Experiments and models have demonstrated that FIWs can even be steered by the geometry of the discharge chamber. For example, one FIW can be split into multiple waves at a the junction of dielectric channels.[9]

The unique characteristics of FIW discharges make them attractive for applications involving large scale production of ultraviolet (UV) radiation,[10] x-rays,[11–15] runaway electrons,[12,16,17] and excited species, such as for lasers[5,18] and plasma assisted combustion.[1,6,19–21] When developing a FIW-based device, one would ideally want to control the spatial distribution of electrons and the electron energy distribution (EED) generated by the FIW as it propagates along the length of the discharge. To achieve these goals, more detailed understanding of FIW development, propagation, and energy deposition would be beneficial.

Many studies to date have used a capacitive probe to measure the electric field and velocity of the FIW wavefront and to calculate axial profiles of electron density.[1,7,8,22] In FIWs sustained in N_2 and air, N_2 emission spectra were

[a)]Electronic addresses: brweathe@gmail.com, zax@esi-group.com, evbarna@sandia.gov, and mjkush@umich.edu
[b)]Present Address: L-3 Communications, Electron Devices Division, 960 Industrial Road, San Carlos, California 94070, USA.
[c)]Present Address: ESI US R&D, 32605 W 12 Mile Road, Suite 350, Farmington Hills, Michigan 48334, USA

measured and correlated with predicted spectra from several models of EEDs. The results were used to identify the shape of EEDs in the FIW, suggesting that the wavefront produces high energy electrons, while lower energy electrons are dominant in the ionized channel trailing behind the FIW.[22] Laser absorption spectroscopy has been used to measure the density of 2^3S He metastables generated by a FIW as a function of time, and the results were compared against a global discharge model.[23] One conclusion of that work was a population of high energy electrons, likely with a non-equilibrium EED, may account for the temporal evolution of metastable density observed in the FIW discharge.

The spatial distribution of emission intensity in these studies is typically not uniform. The emission intensity is peaked on axis for some conditions, while for others, the emission is most intense near the walls of the discharge chamber.[2] The type of gas and the polarity of the pulse both influence the radial distribution of the optical emission.[1]

The goal of the investigations discussed in this paper is to build upon these prior works to improve our understanding of spatial profiles in FIW discharges. The experimental work involved temporal and spatial measurements of electron and metastable atom densities in FIWs sustained in He for pressures of a few to tens of Torr. These measurements were made using laser-induced fluorescence (LIF) and laser collision-induced fluorescence (LCIF) diagnostics. The trends of these profiles were compared with predictions from fluid-based simulations and discussed in the context of the underlying processes in FIWs. The results show that the spatial distribution of electron and metastable densities, the peak electron density, and the wave velocity trend similarly with pressure. At low pressure, profiles of densities are center-peaked, while at high pressure, the densities peak near the wall. At intermediate pressures, densities and wave velocities are highest and the discharge is most uniform. Simulations show that the electric field in the wavefront, which shapes the ionization rate, may be enhanced locally at the walls or on axis, depending on the pressure.

The experiment is discussed in Sec. II and an overview of the model is provided in Sec. III. Measurements of electron density and metastable atom density profiles are discussed in Sec. IV and those predicted by the model are discussed in Sec. V. Concluding remarks are in Sec. VI.

II. DESCRIPTION OF THE EXPERIMENT

A schematic of the FIW apparatus is shown in Fig. 1. The discharge was sustained within a cylindrical glass tube, 25.4 cm long, with an inner diameter of 3.3 cm and wall thickness of 0.24 cm. Each end of the glass tube was terminated by a cylindrically symmetric stainless steel electrode assembly. Both electrodes had an inner diameter of 3.6 cm. The high voltage assembly was 15.2 cm long and the grounded assembly was 5.5 cm long. The high voltage electrode was surrounded by a 24.5 cm long poly-tetrafluoroethylene (PTFE) cylinder, with inner and outer diameters of 7.1 and 10.8 cm. The PTFE cylinder was wrapped with a copper sleeve, capped on each end by aluminum plates. An aluminum tube with an inner diameter of 7.3 cm was mounted around the glass tube, with a slot to allow for optical access to the discharge. This aluminum shield was in electrical contact with the downstream electrode via a copper shim and was also in contact with the shielding surrounding the PTFE sleeve. The shielding for the high voltage, the aluminum tube, and the downstream electrode were grounded.

Helium was fed into the chamber through insulating tubing connected to the high voltage electrode. Downstream of the grounded electrode, the discharge chamber was mounted to a vacuum pumping system through a second glass tube. The chamber was evacuated by a rotary vane pump with a peak pumping speed of 5.2 L/s, and the He flow rate was varied from 10 to 50 sccm with a mass flow controller. The internal helium pressure was controlled by the flow rate and a set of throttling valves between the chamber and the pump. The base pressure was $<10^{-3}$ Torr and the leak rate of room air was limited to 1.7×10^{-5} Torr/s. From the leak rate, the maximum impurity level of room air is estimated at 0.03%. A high voltage nanosecond pulse generator (ANVS Model PT510NMS) was connected to the high voltage electrode by the center conductor of a RG-213 coaxial cable, while the outer conductor of the cable connected the external shielding of the discharge chamber to ground. The cable was 15.4 m in

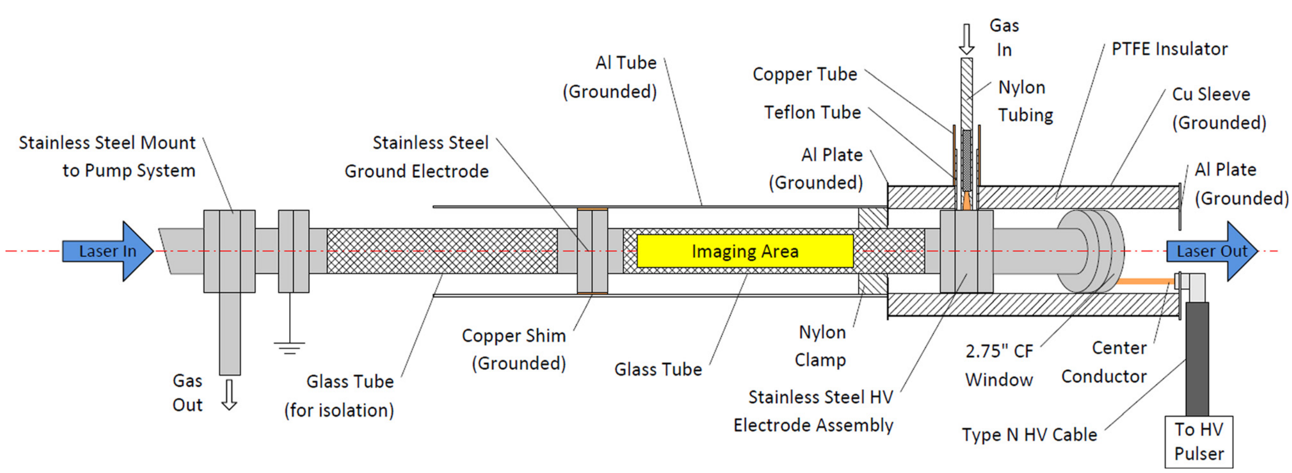

FIG. 1. Schematic of FIW discharge chamber.

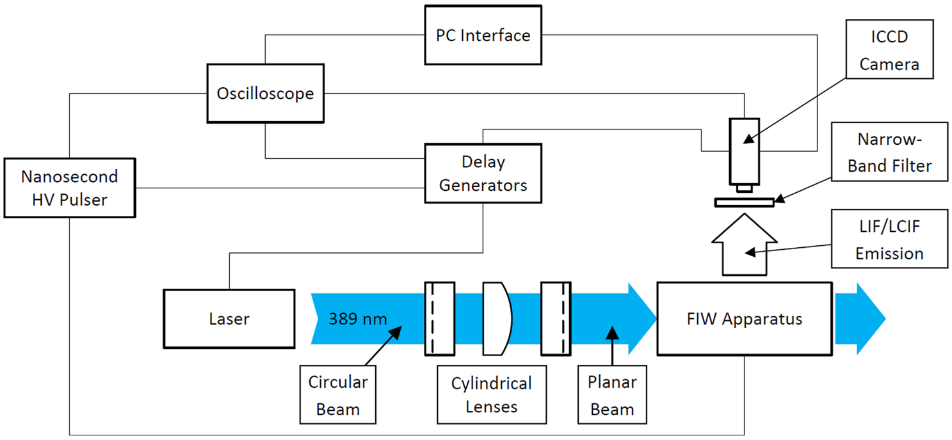

FIG. 2. Layout of optical diagnostics.

length, which was sufficiently long that at the high voltage electrode, secondary pulses due to reflections at the pulser could be separated from the incident pulse. The pulse separation between the incident and reflected waves measured at the nanosecond pulse generator was >120 ns. The pulse generator was used to apply pulses of 14 kV (open load), with a typical rise time of 2–3 ns and pulse width of 25 ns at a repetition rate of 1 kHz.

The setup for the LIF and LCIF measurements is shown in Fig. 2. The third harmonic (355 nm) of a Nd-YAG laser was used to pump an optical parametric oscillator (OPO) and frequency doubling system at 20 Hz with a pulse duration of ≈5 ns. The OPO was tuned to produce a beam with a wavelength of 388.9 nm, corresponding to the $2^3S \rightarrow 3^3P$ transition in He. The laser energy per pulse was regulated by a rotating polarizer and quarter wave plate, and the output laser beam was shaped into a planar sheet by a series of irises, focusing optics, and cylindrical lenses. The final beam width was ≈1 mm.

The planar beam was aligned to illuminate a radial cross-section of the discharge tube centered on the axis. An intensified charge-coupled device (ICCD) camera was used to record images of the illuminated plane. Interchangeable narrow-band filters (≤10 nm bandwidth) were used to isolate emission from each transition of interest. The distortion of the image due to the glass tube was not significant. The laser, ICCD, high voltage pulser, and oscilloscope were triggered by a synchronized set of digital delay generators. An oscilloscope was used to monitor the high voltage waveforms at the pulser, the laser pulse time via a fast photodiode, the ICCD gate pulse, and the line-averaged emission detected by a photomultiplier tube near the discharge chamber. The oscilloscope waveforms, images, ICCD settings, and delay generator settings were digitally recorded and stored for later analysis. An example of the voltage waveform is shown in Fig. 3, along with the temporal window between the forward and reflected pulses in which the LCIF measurements were made.

Relative densities of He atoms in the 2^3S metastable state were imaged using LIF, while absolute measurements of electron density were mapped using 2D-LCIF, as described by Barnat and Frederickson.[24] A schematic of the LCIF pumping scheme is shown in Fig. 4. The laser pulse is used to transfer a portion of the He 2^3S metastable population to the 3^3P state. Collisions by electrons in the plasma redistribute the laser excited He atoms in the 3^3P state to nearby electronic states, which then decay by optical emission, comprising the LCIF signal. By normalizing the intensity of emission from these collisionally excited states to that of LIF emission from the 3^3P state, one can determine the electron density and temperature, T_e, for a particular EED. Over a range of electron densities from 10^9 to $10^{13}\,\mathrm{cm}^{-3}$, the

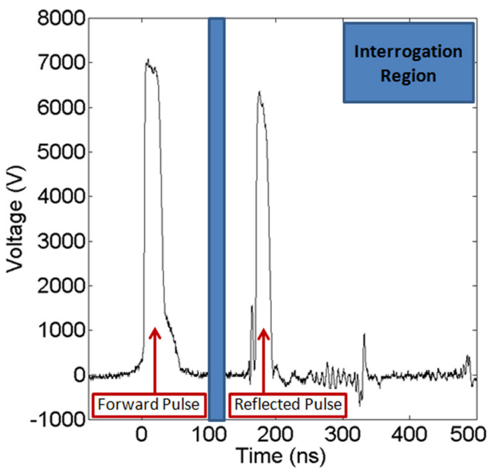

FIG. 3. Sample high voltage waveform as measured at the HV pulser monitor, showing forward and reflected voltage pulses and the temporal interrogation window for LCIF measurements.

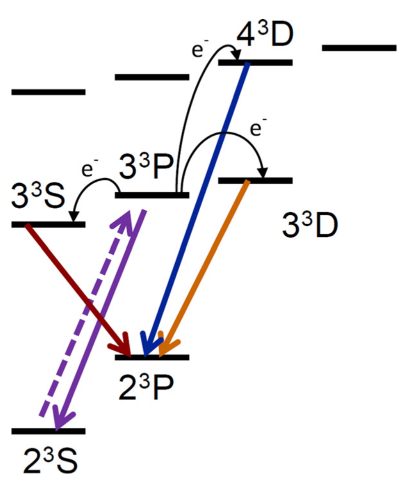

FIG. 4. Optical pumping scheme for the LCIF diagnostic.

time-integrated ratio of LCIF emission at 587.5 nm ($3^3D \rightarrow 2^3P$) to LIF emission at 388.9 nm ($3^3P \rightarrow 2^3S$) varies linearly with electron density, being nearly independent of electron temperature. This insensitivity to T_e results, in part, because the energy differential between the two upper states (0.067 eV) is much less than the typical value of T_e (a few eV). In order to correlate these ratios of emission to absolute quantities, a collisional radiative model (CRM) is needed, which accounts for spontaneous, electron collision-driven, and atomic collision-driven transitions. For this study, the results from the CRM discussed in Ref. 24 were used.

For a given measurement, the delays between the ICCD, laser pulse, and high voltage (HV) pulser, as well as the ICCD gate duration, were held constant during the imaging of each transition. An image of a given transition was recorded with and without the laser beam, and the plasma induced emission (PIE) was subtracted out of the LCIF images. Up to 20 images of each transition were averaged, with each transition having a variable total accumulation time to vary the signal strength as needed. The ratios of the corrected and averaged images were then compared to the results from the CRM at each position to generate a spatial map of electron density. For this measurement technique to yield useful results, the FIW must be repeatable for each pulse. The LCIF intensities recorded by this procedure varied by less than 5 percent from shot to shot, and the maximum jitter between the laser diagnostics and the HV pulse was $\leq$5 ns.

III. DESCRIPTION OF THE MODEL

The numerical modeling platform used in this study is *nonPDPSIM*, a two-dimensional plasma hydrodynamics model with radiation-photon transport. It is essentially the same model used for the investigation of FIWs in a rectangular channel as discussed in Ref. 1. Continuity equations for charged and neutral species, and Poisson's equation for electric potential, are solved coincident with the electron energy equation with transport coefficients obtained from solutions of Boltzmann's equation. Photon transport is based on a propagator or Green's function method, which accounts for intervening absorption and obstructions. The spatial discretization is based on finite volume method using an unstructured mesh. The time integration is implemented with a fully implicit Newton iteration method.

For the experimental setup shown in Fig. 1, the simulations were performed in an axisymmetric discharge configuration, which includes the glass discharge tube, the grounded aluminum tube, the copper sleeve, the stainless steel HV and grounded electrodes, the Nylon clamp, the PTFE insulators, and the ambient air ($\varepsilon_r = 1$). The unstructured computational grid has a total of 18 000 nodes with about 13 500 located inside the plasma zone. The computational domain extends 10 cm in radius and 55 cm in length, though only the relevant subset of the computation domain is shown in the results. The discharge tube is filled with He at 1–20 Torr with a trace impurity represented by O_2 at the level of 0.1%. The species included in the model are ground states of He(^{1}S) and O_2, excited helium states, He(2^3S), He(2^1P), He(3^1P), and the excited helium dimer He_2*. The charged species included are He^+, $He_2{}^+$, $O_2{}^+$, and the electron e. The reaction mechanism is discussed in Refs. 25 and 26. The photoionization of O_2 by the UV light from the radiative He(2^1P) provides seed electrons ahead of the ionization front, which for the positive FIW, enables the ionization wave to propagate in the absence of preionization. The photo-ionization cross-section for O_2 is set at $5 \times 10^{-16}\,\mathrm{cm}^{-2}$. The secondary electron emission coefficients from the plasma bounding surfaces by ion and photon bombardment are $\gamma = 0.15$ and $\gamma_p = 0.01$, respectively. Parameterization of the secondary emission coefficients showed that the results for, for example, the speed of the FIW were not particularly sensitive to secondary emission for the range of $\gamma = 0.01$ to 0.15. The initial electron density is $10^8\,\mathrm{cm}^{-3}$, uniformly distributed inside the discharge tube. Although, in general, the FIW speed increases with initial electron density, in the experiments discussed here, the speed of the FIW is determined predominately by the photoionization process. We found that the initial electron density has little effect on the FIW speed as long the initial density is less than $10^9\,\mathrm{cm}^{-3}$.

The voltage waveform measured experimentally at the pulser (7 kV peak) is used to set the simulated voltage pulse shape. Since the discharge chamber is initially a mismatched (open) load, a simulated pulse of 14 kV is used. To approximate the HV pulse shape in the experiments, the simulated pulse has a pulse length of 20 ns with a 2.5 ns rise time and 7.5 ns decay time. The total simulation time is 300 ns. Only a single pulse for each condition is addressed by the model. Estimates and measurements of, for example, the He metastable density at the end of the 1 ms interpulse period are sufficiently low that we can consider each pulse independently.

The trace amount of O_2 used in the simulation is intended to represent the unknown species that is photoionized in the experiments. In general, the FIW speed increases with the trace O_2 density. The O_2 density used in the simulation was determined based on two criteria. First, the O_2 density must be within the specified impurity limit of the plasma gas used in the experiment. Second, within this limit we chose an impurity level and photoionization cross section so that the computed FIW dynamics matched the experiments at one pressure. These values were then fixed for the other pressures.

IV. MEASUREMENTS OF ELECTRON DENSITY IN FIWs

Metastable and electron density profiles were measured at different pressures with all other parameters held constant. A 14 kV pulse was applied at a repetition rate of 1 kHz, and the pressure was varied between 1 and 20 Torr. At each pressure, images with a gate width of 20 ns were taken at a fixed delay of 100 ns ($\pm$5 ns) after the initial detection of plasma-induced emission. At these pressures, the diffusion loss time of electrons in He requires several to tens of microseconds. As a result, the spatial distribution of electron density is little changed over the time duration of the measurement, and represents a snapshot of where the plasma was initially generated by the FIW. The measured electron densities are shown

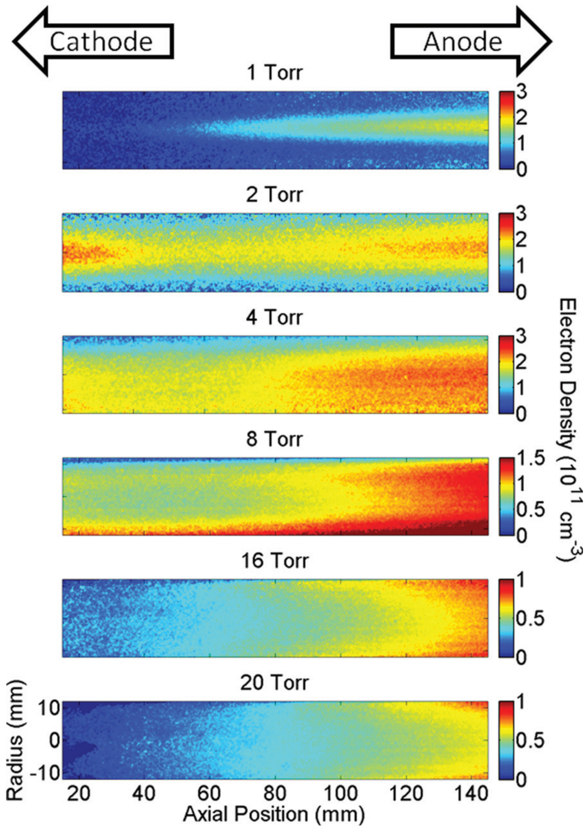

FIG. 5. Images of absolute electron density, in units of 1011 cm^{-3}, at different pressures, taken 100 ns after the high voltage pulse with a 20 ns ICCD gate. HV anode and grounded cathode are located at positions of 140 mm and 0 mm, respectively.

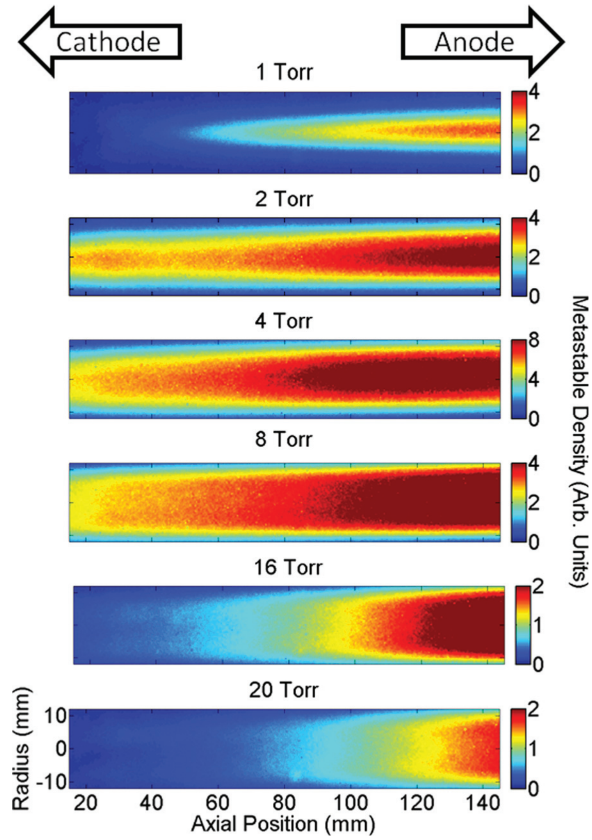

FIG. 6. Images of relative metastable He atom density (in arbitrary units), taken 100 ns after the high voltage pulse, with a 20 ns ICCD gate. HV anode and grounded cathode are located at positions of 140 mm and 0 mm, respectively.

in Fig. 5 and measured metastable atom densities are shown in Fig. 6. The anode is to the right of these images, and the grounded electrode is to the left (at the axial position of 0 mm). Corresponding one-dimensional radial profiles at an axial position of 140 mm are shown in Fig. 7.

The FIW is always initiated at the high voltage electrode, consistent with prior studies on both positive and negative polarity discharges.[1,8,27] The wave then propagates toward the grounded electrode. Depending on the discharge conditions, the FIW can either traverse the entire anode-cathode gap or be attenuated along the length of the tube. Since total current is conserved along the length of the coaxial discharge tube, current is carried by the plasma (dominantly by the electrons) along the ionized channel, while current in the non-ionized portion is carried by displacement current.[2] At 100 ns after the pulse, in all cases, the maximum electron density is $\approx 10^{11}$ cm^{-3}. This delay between the onset of voltage and the measurement is sufficiently long that the FIW has already passed when the images are taken. To confirm that the electron density distributions were unchanged during the diagnostic, a set of LCIF measurements were taken at variable delays of 20–100 ns after the FIW pulse. The shapes of the density profiles, and maximum values, did not significantly change. Therefore, these profiles provide an integrated footprint of the production of electrons and metastable states by the FIW as it traversed the tube.

There is a clear dependence of the FIW radial distribution on the pressure. At 1 Torr, both the electron and metastable atom densities are peaked on axis, and are attenuated along the length of the gap. As the pressure is increased to 2 and 4 Torr, the profiles of both species are broadened and the discharge completely traverses the gap. Further increases in pressure from 8 to 20 Torr resulted in electron densities that are peaked near the walls of the discharge tube. At the same pressures, the metastable atom density profiles are flattened, indicating that metastable production is also shifted away from the axis. Although the transition to a wall-hugging distribution at high pressure is more pronounced for electrons than for metastables, both species show the same trend with pressure. Accompanying this trend at high pressure is an increase in the attenuation of the wave in the axial direction, along with a decrease in the peak densities of both species.

These images suggested a general trend of the densities of both species shifting from center-dominated to wall-hugging profiles as the pressure increases. Maximum electron and metastable atom production occurs at about 4 Torr, which is also the pressure at which the attenuation of the wave is at a minimum and the discharge fills the largest volume of the tube. The shift from a center-dominated profile to a wall-hugging profile also occurs at about 4 Torr. For a given axial location, regions of high electron and metastable atom densities near the wall indicate that production rates

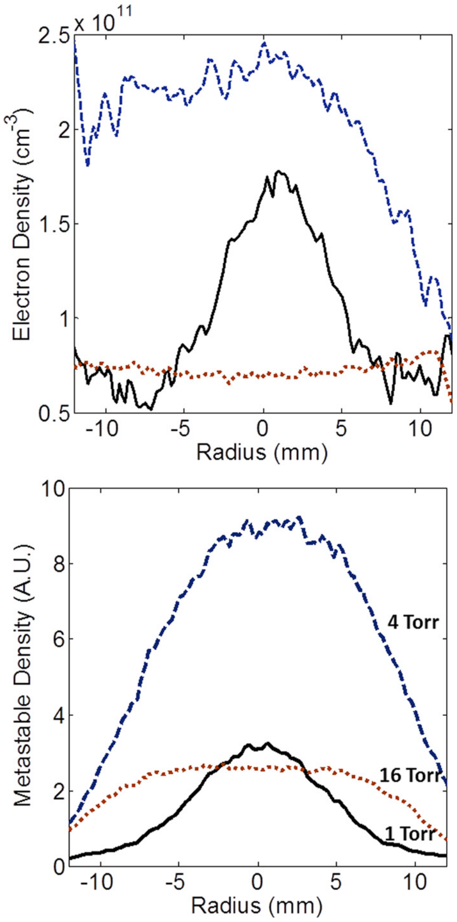

FIG. 7. Radial profiles of electron density (upper plots) and relative He metastable atom density (Lower plots) 140 mm from the ground electrode and for pressures of 1 Torr (solid black line), 4 Torr (dashed blue curve), and 16 Torr (dotted red curve).

are also highest at the wall. These measurements of the radial distributions of electron and metastable atom densities qualitatively agree with optical emission measurements performed by Vasilyak *et al.*[2] In that study, images (without spectral resolution) were taken of a 30 kV FIW discharge in N_2, using an exposure time of 1.5 ns. The images showed a center-peaked wavefront at 1–4 Torr, transitioning to a wall-peaked wavefront at 12 Torr and above.

The cause of the asymmetries observed in the electron densities (Figures 5 and 7) for both the 4 Torr case and the 8 Torr case is unknown. While artifacts introduced by the measurement procedure cannot be ruled out, the symmetric profiles observed at both higher and lower pressures indicate that such artifacts are not likely. Therefore, it is likely that there is some mechanism that induces the asymmetric electron distribution in the plasma discharge. One such mechanism could be slight asymmetric coupling of the electric fields to the outer grounded shell. In a recent study looking the distribution of longer-pulsed plasma discharges, similar asymmetries were observed in the distribution of the plasma as conditions (such as E/N) approached a values that favored one distribution over another.[28] Single-shot snapshots of plasma density further indicate that the plasma is unstable near these transitions and may be particularly sensitive to modest asymmetries present in the experiment.

The velocity of the wavefront of the FIW was estimated by imaging (with a 2 ns gate), the plasma induced emission (PIE) of the 389 and 588 nm lines from excited He without the LIF laser pulse, while the ICCD delay was varied from 2 to 20 ns after the FIW was launched. Time $t = 0$ was defined as the earliest time that any PIE was observed by the ICCD. Axial profiles of PIE intensity on centerline were extracted from the 2-D images. Ahead of the wavefront, the background intensity was negligible relative to the peak intensity. The wavefront position at each time was defined by the location of fixed values of emission intensity, depending on the transition being imaged, and tracking the location of this intensity as a function of time. Average wavefront velocities were calculated from the change in wavefront position between two subsequent frames and the associated time step. The wavefront velocity as a function of distance from the anode for different pressures is shown in Fig. 8. Velocities were not determined for pressures above 8 Torr due to weak levels of PIE downstream of the high voltage electrode.

At all pressures, the speed of the wavefront gradually decreases as the wave travels along the tube. The voltage applied to the anode is divided between the non-ionized gas ahead of the ionization front, the ionization front itself, and the plasma column trailing the ionization front. The respective voltage drops are proportional to their relative resistances. Generally, the maximum E/N (electric field/gas number density) occurs across the wavefront. In this region, there is significant charge separation, which induces a large voltage drop across a narrow region of space. A smaller residual electric field occurs in the plasma column between the wavefront and the anode. The decrease in the velocity of the wavefront with distance from the anode is likely due to the finite conductivity and associated voltage drop of the plasma column trailing the ionization front, which then reduces the available voltage (and E/N) to sustain the ionization wave. As the ionization front propagates further from the anode, the voltage drop across the plasma column increases, which then reduces the E/N in the wavefront, which, in turn,

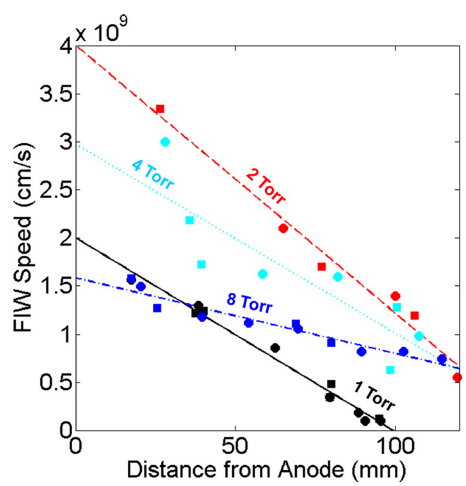

FIG. 8. Wavefront speed as a function of distance from anode, at 1 to 8 Torr. Circles mark points calculated from 389 nm emission; squares mark points calculated from 588 nm emission.

reduces its speed. There may also be some geometrical electric field enhancement at the anode, which locally increases the speed of the wave. At 1 Torr, the speed of the wavefront is largest near the anode and drops to zero at 40 mm prior to reaching the ground electrode. This location corresponds to the tip of the electron and metastable density profiles at 1 Torr is shown in Figs. 5 and 6. At 8 Torr, the speed of the wave is attenuated, but to a lesser degree. In this case, the wave traverses the entire gap in agreement with the measured density profiles imaged after 100 ns.

The differences between the speeds of the waves at the two extremes (1 Torr and 8 Torr) are explained by the mechanism of FIW propagation. In propagation of a positive FIW, the electric field accelerates electrons towards the anode in the opposite direction of propagation of the wave. To advance the wave, there must either be a pre-existing electron density ahead of the wavefront, or a mechanism for producing free electrons ahead of the wavefront, such as photoionization.[7] When the positive high voltage pulse is applied, available electrons slightly ahead of the wavefront are accelerated towards the anode, generating an anode directed avalanche. The electrons resulting from the avalanche shield out the applied potential from the anode. The low mobility ions produced during the avalanche are essentially motionless during this process, which then results in space charge separation and its associated voltage drop, which sustains the FIW moving away from the anode. The speed of wave propagation is in part determined by the availability of back-streaming electrons through ionization and the speed with which they can move to shield the positive potential.

At low pressures (1 Torr), the electrons are mobile and can readily drift towards the anode. However, the rate of ionization at the low pressure is small, so the conductivity of the plasma channel behind the ionization front builds relatively slowly. This results in a relatively large voltage drop across the plasma column, which reduces the E/N in the ionization front and eventually causes the wave to stall. At this point, current continuity is produced by displacement current ahead of the ionization front.[2] As the pressure increases, the rate of ionization also increases, and a plasma column is produced behind the ionization front with lower conductivity than at lower pressures. This makes more voltage available for avalanche in the ionization front, which enables the plasma column to be further extended along the column during the applied pulse. However, as more energy is dissipated through collisions, the increasing neutral density overtakes the increasing electric field in the wavefront, and eventually E/N decreases. This then decreases both the ionization rate and electron drift speed into the wavefront, which decreases the propagation speed of the wavefront.[2] For this discharge, pressures near 4 Torr correspond to where these two processes, ionization and mobility, are in balance with one another so that the electrons are produced in large number and can rapidly move to shield out regions of positive potential. Exactly specifying this pressure dependence for a specific experimental setup is difficult because the FIW properties depend on additional parameters such as geometry, gas species, pre-pulse electron densities, and dielectric properties of the chamber.[7] However, the same qualitative trends have been observed in other experiments.[2,29]

V. SIMULATIONS OF FIW PROPERTIES

The experimental parameters were used as initial conditions for the model over a range of pressures from 1 to 20 Torr. The resulting electron densities are shown in Fig. 9 at 120 ns after the start of the voltage pulse. The total ionization rates at different times up to 120 ns are also shown. The volume that was experimentally imaged is bounded by the dotted lines. The results from the simulation capture several of the experimentally observed characteristics of the FIW discharge. The overall trends of electron densities transitioning from center-peaked to wall-hugging from low to high pressure are reproduced. At 1 Torr, the peak electron density in the imaged region is the lowest relative to the other pressures, with a calculated value of $4 \times 10^{10}\,\mathrm{cm}^{-3}$. This compares to $1.5 \times 10^{11}\,\mathrm{cm}^{-3}$ in the experiment. Note that the absolute maximum in electron density occurs closer to the anode, $5 \times 10^{10}\,\mathrm{cm}^{-3}$, outside of the imaged region. The maximum electron density is predicted to occur at an intermediate pressure of 4 Torr and then decreases at pressures up to 20 Torr ($1.5 \times 10^{12}\,\mathrm{cm}^{-3}$ at 20 Torr), as in the experiment. These predicted maxima sometimes occur outside the imaged volume; however, the trend inside the imaged volume is the same. The maximum electron densities at each pressure in the imaged region are within a factor of 3–4 of that observed experimentally. The differences may be due to uncertainties in the impurity concentrations in the gas and the degree of preionization or excited states present from prior pulses before the HV pulse.

As in the experiment, the speed of the FIW decreases with distance from the anode. The average wave speed across the gap at 8 Torr is $0.74 \times 10^9\,\mathrm{cm\ s}^{-1}$, which is maximum in the pressure range surveyed in this study. A comparison between model and experimental results for the FIW speed, v_f, 80 mm from the anode is shown in Fig. 10. At 1 Torr, $v_f = 0.2 \times 10^9\,\mathrm{cm\ s}^{-1}$ and in the experiment $v_f = 0.4 \times 10^9\,\mathrm{cm\,s}^{-1}$, which is insufficient for the FIW to propagate from anode to cathode during the 25 ns voltage pulse. In the model results, v_f increases up to 8 Torr to $1.0 \times 10^9\,\mathrm{cm\ s}^{-1}$ at which point the wave speed is nearly constant, perhaps decreasing slightly. The model agrees with the high pressure value of v_f measured in the experiment but does not capture the maximum in v_f at intermediate pressures (2 and 4 Torr). The trends from the model agree with the LCIF measurements, which show little change in the FIW structure after the wave passes, as well as those in Fig. 5, wherein the wave stalls before closing the gap at 1 Torr. The cause for the disagreement in v_f at intermediate pressures has not been precisely determined. It is known that the FIW speed will increase with increasing initial values of electron density. The prepulse electron density was held constant at $10^9\,\mathrm{cm}^{-3}$ in the model over all pressures. It may be that this value varies as a function of pressure.

The total ionization source, S_e, at different times during the pulse is shown below the electron density for all pressures in Fig. 9. Note that since S_e varies by many orders of magnitude during the 120 ns, S_e is separately normalized in each

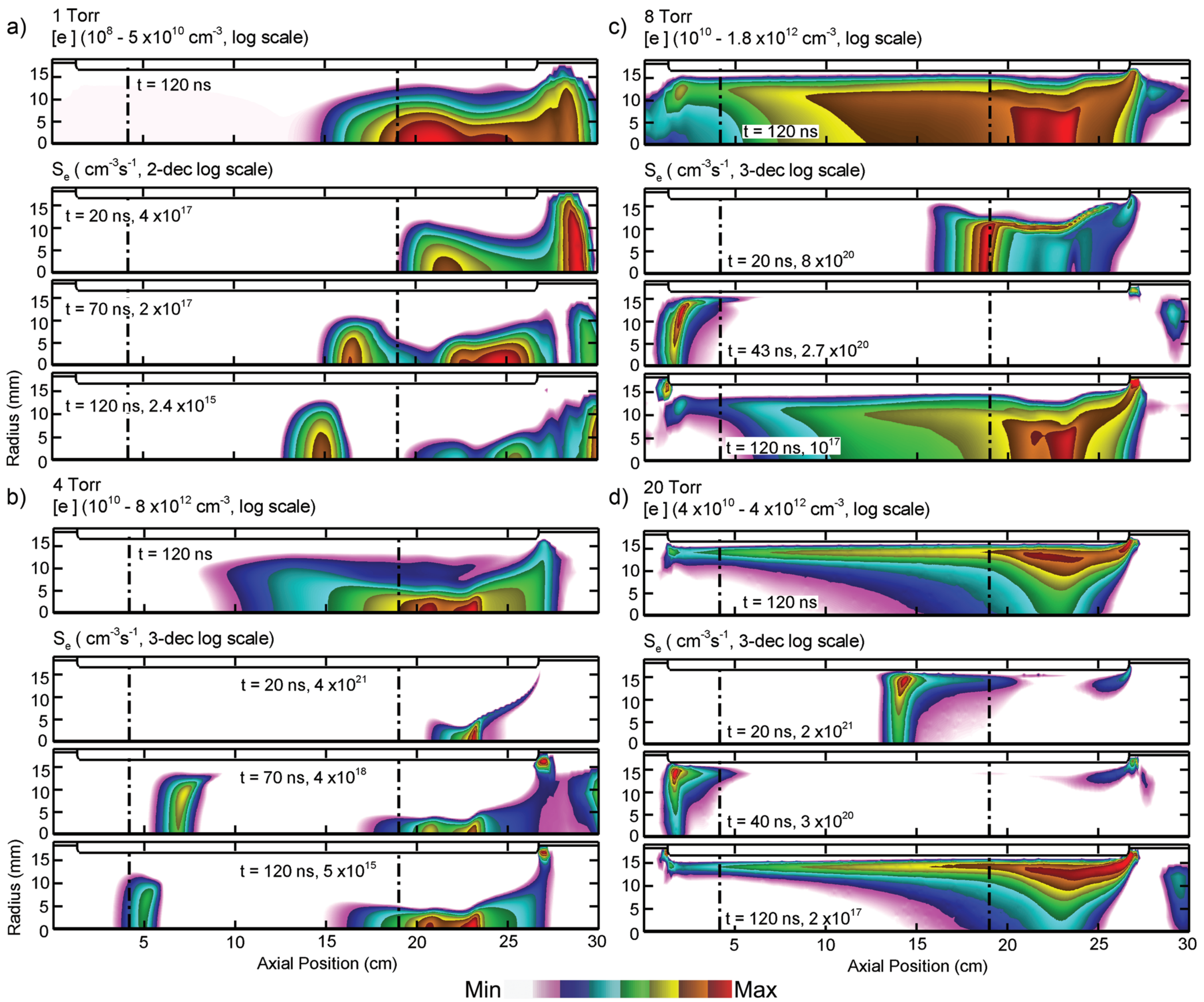

FIG. 9. Results from the model for electron density profile (top of each subfigure) and ionization source rate at three different times. Results are shown for 1, 4, 8, and 20 Torr. Dashed lines indicate the experimentally imaged region.

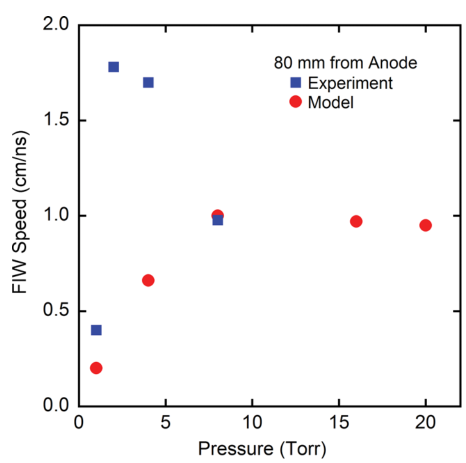

FIG. 10. Comparison of FIW speed at 80 mm from the anode between the model and experiments.

frame. In all cases, S_e is at the maximum in the wavefront itself, as best seen in the 1 Torr case. At 1 Torr, the maximum value of S_e in the wavefront is $3.9 \times 10^{17}\,\mathrm{cm^{-3}s^{-1}}$. Behind the wavefront in the plasma column, S_e decreases by a factor of 2.

Note that even though the voltage on the anode goes to zero by 60 ns, the ionization wave continues to propagate, with decreasing values of S_e, for as long as 50 ns after termination of the voltage pulse. The fact that S_e is non-zero after the voltage is removed is not surprising. The electron temperature has a finite rate of thermalization and so ionization of excited states continues while some electron heating continues due to superelastic relaxation of the He excited states. Ionization also continues through Penning processes. The unexpected result is that S_e continues to propagate in space away from the high voltage electrode after the voltage on the anode is turned off. This propagation is sustained by the potential energy that is stored in space charge, producing the plasma potential and charging of the side walls. The plasma potential in the discharge after the high voltage is switched off is shown in Fig. 11.

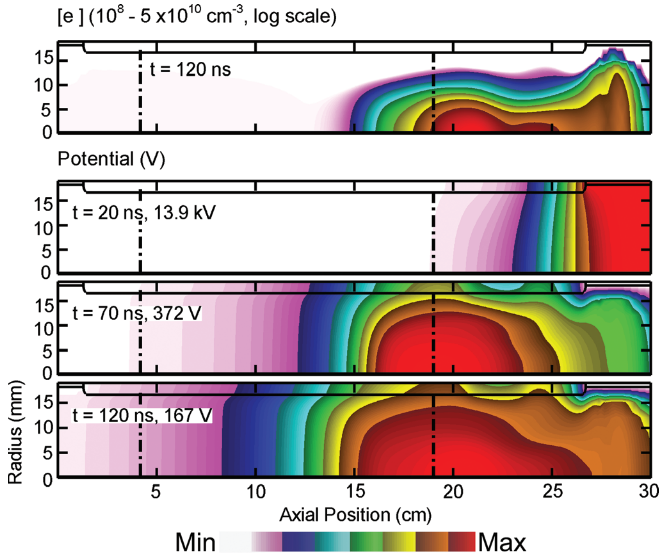

FIG. 11. Simulated profiles of electron density (top) and plasma potential for three different times, at 1 Torr.

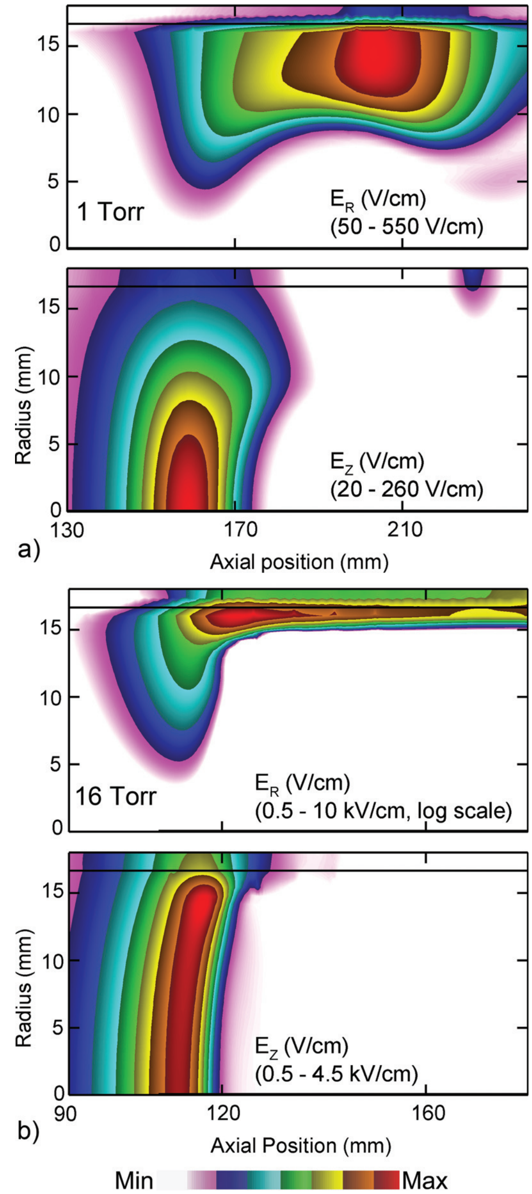

FIG. 12. Simulated contours of instantaneous (a) radial and (b) axial electric field within the FIW front, at 1 Torr and 16 Torr.

As the pressure increases, S_e transitions from propagating along the axis to following the walls of the chamber. The source of this transition is, in part, a consequence of the electron mean free path, and partly a consequence of electric field enhancement, either at the dielectric wall or on the axis. In prior studies of dielectric barrier discharges and the inside of bubbles in liquids, spreading of plasmas along dielectric surfaces is partly explained by the electric field enhancement that occurs at the interface between the conductive plasma with $\varepsilon/\varepsilon_0 \approx 1$ and the non-conductive boundary having a large $\varepsilon/\varepsilon_0$ (in this case, $\varepsilon/\varepsilon_0 = 4.7$).[30,31] The low conductivity of the dielectric enables charge accumulation on the surface, which further intensifies the electric field.

At low pressure, the mean free path of electrons is large enough to transport electron energy from the wall towards the axis of the plasma. Once the plasma forms along the axis, it has the electrical appearance of being a conductive column with a small terminating radius of curvature, and so there is electric field enhancement, which helps to propagate the FIW along the axis. The importance of curvature of the head of the FIW and the resulting electric field enhancement has been discussed in the context of atmospheric pressure FIWs.[31] If the time to conduct the electron energy from the wall to the axis is small compared to the transit time of the FIW, the electric field enhancement on axis is dominant and the FIW propagates along the axis.

As the pressure increases, the mean free path of the electrons decreases, and the heating of electrons by the electric field enhancement at the walls remains local. The radial convection (or conduction) of electron energy is sufficiently slow compared to the axial speed of the FIW that the FIW propagates dominantly along the wall. These trends are shown in Fig. 12, where the radial, E_r, and axial, E_z, components of the electric field are shown for 1 Torr (58 ns) and 16 Torr (20 ns). These times correspond to roughly the quasi-steady propagation period within the experimental observation window. At 1 Torr, the axial electric field in the wavefront that is responsible for propagation of the FIW is 50 V/cm (7.8×10^{-15} V cm^2 or 780 Td) and is peaked along the axis. The radial electric field is about twice as large and peaks at the surface. In contrast, at 16 Torr, the axial field is more uniform along the inner diameter of the tube, and peaks at the wall at 4 500 V/cm (8.7×10^{-15} V cm^2 or 870 Td). The more conductive plasma in the vicinity of the wall compresses the radial electric field towards the wall, increasing its maximum value to 11 kV/cm (2.1×10^{-14} V cm^2 or 2100 Td).

The radial electric field, E_r, is maximum at the wall for both pressures. In the high pressure case, E_r decreases rapidly away from the wall due to the high conductivity of the wall hugging plasma. The electric field can be described by two distinct regions—the leading edge of the FIW, where the axial field, E_z, is significant; and the region behind the wavefront, where electric fields are concentrated near the wall and have a dominantly radial orientation. This latter region corresponds to the conductive plasma column behind the FIW and

E_r in large part results from the sheath and surface charging. At 1 Torr, the two electric field regions are quite distinct. At 16 Torr, the nearly uniform E_z across the radius overlaps with the region of peak E_r near the wall. The end result is that the maximum total electric field in the wavefront region occurs on centerline at the lower pressure, and near the wall at the higher pressure. This translates directly to the ionization rate profiles shown in Fig. 8, producing the observed electron density profiles.

VI. CONCLUDING REMARKS

Two-dimensional profiles of electron density and metastable states in FIW sustained in helium were investigated using LIF and LCIF spectroscopy. The general observation is a transition of plasma density from the axis to the walls with increasing pressure. Results from modeling correlate this transition in plasma density with a transition of the electric field distribution from the axis to the walls, which, in turn, determines the rates of ionization. Measurements of FIW velocities and maximum plasma densities suggest that for a given electrode configuration and dielectric properties of the tube, there is an optimum operating pressure at which spatially uniform discharges can be achieved. This pressure also correlates to the conditions, which produce the maximum FIW speed and electron density.

The model shows that the FIW continues to propagate even after the high voltage pulse is removed from the powered electrode. The radial distribution of the axial electric field depends on two factors—the rate of energy transport from the walls to the centerline (dictated by pressure) and local electric field enhancement at the location of the wavefront. At low pressure, energy is rapidly transported from the wall to the centerline. Once a conductive plasma column is established on axis, the electric field is intensified at the tip of the plasma column, which drives further ionization on axis. At high pressure, energy is transported slowly from the wall. As the FIW propagates more quickly relative to the rate of energy transport, the region of peak electric field then is confined to the wall, and is locally enhanced by the dielectric constant of the glass and charging of the surface. It is the redistribution of the location of the peak electric field as a function of pressure that causes changes in the radial distribution of ionization and excitation observed in FIW discharges.

The FIW discharge represents a challenging system to both diagnose as well as to simulate. While close coordination between experiment and simulation was maintained, differences between the results for the two approaches were clearly observed. Direct one-to-one comparison between simulation and experiment is complicated by the inability to assess small but potentially important unknowns. The amount and nature of trace impurities present the experimental configuration, uncertainties in electron emission from the walls and the residual charge present in the chamber prior to the launching of the FIW have significant impact on the dynamics of the discharge. Furthermore, deviations from an ideal setup such as slight asymmetries in capacitive coupling between the plasma and ground planes or more subtle interactions giving rise to instabilities can lead to factors such as the asymmetric profiles observed in the electron densities. A controlled assessment of these factors would not only further the ability to directly compare simulation to experiment, but enhance our understanding on how these subtle details govern FIW dynamics.

ACKNOWLEDGMENTS

This work was supported by the Department of Energy Office of Fusion Energy Sciences Contract No. DE-SC0001939.

[1]K. Takashima, I. V. Adamovich, Z. Xiong, M. J. Kushner, S. Starikovskaia, U. Czarnetzki, and D. Luggenholscher, Phys. Plasmas **18**, 083505 (2011).
[2]L. M. Vasilyak, S. V. Kostyuchenko, N. N. Kudryavtsev, and I. V. Filyugin, Phys. Usp. **37**, 247–269 (1994).
[3]S. M. Starikovskaia, N. B. Anikin, S. V. Pancheshnyi, D. V. Zatsepin, and A. Y. Starikovskii, Plasma Sources Sci. Technol. **10**, 344–355 (2001).
[4]A. N. Lagarkov and I. M. Rutkevich, *Ionization Waves in Electrical Breakdown of Gases* (Springer-Verlag, New York, 1994).
[5]A. Hicks, S. Tirupathi, N. Jiang, Y. Utkin, W. R. Lempert, J. W. Rich, and I. V. Adamovich, J. Phys. D: Appl. Phys. **40**, 1408–1415 (2007).
[6]I. V. Adamovich, I. Choi, N. Jiang, J.-H. Kim, S. Keshav, W. R. Lempert, E. Mintusov, M. Nishihara, M. Samimy, and M. Uddi, Plasma Sources Sci. Technol. **18**, 034018 (2009).
[7]E. I. Asinovsky, A. N. Lagarkov, V. V. Markovets, and I. M. Rutkevich, Plasma Sources Sci. Technol. **3**, 556–563 (1994).
[8]N. B. Anikin, S. M. Starikovskaia, and A. Y. Starikovskii, J. Phys. D: Appl. Phys. **35**, 2785–2794 (2002).
[9]Z. Xiong, E. Robert, V. Sarron, J.-M. Pouvesle, and M. J. Kushner, J. Phys. D: Appl. Phys. **45**, 275201 (2012).
[10]S. V. Pancheshnyi, S. M. Starikovskaya, and A. Y. Starikovskii, Plasma Phys. Rep. **25**, 393–397 (1999).
[11]R. C. Noggle, E. P. Krider, and J. R. Wayland, J. Appl. Phys. **39**, 4746–4748 (1968).
[12]L. P. Babich, T. V. Loiko, and V. A. Tsukerman, Sov. Phys. Usp. **33**, 521–540 (1990).
[13]V. B. Bratchikov, K. A. Gagarinov, I. D. Kostyrya, V. F. Tarasenko, A. N. Tkachev, and S. I. Yakovlenko, Tech. Phys. **52**, 856–864 (2007).
[14]C. Zhang, T. Shao, Y. Yu, Z. Niu, and P. Yan, Rev. Sci. Instrum. **81**, 123501 (2010).
[15]A. V. Kozyrev, V. F. Tarasenko, E. K. Baksht, and Y. V. Shut'ko, Tech. Phys. Lett. **37**, 1054–1057 (2011).
[16]S. B. Alekseev, V. M. Orlovskii, V. F. Tarasenko, A. N. Tkachev, and S. I. Yakovlenko, Tech. Phys. Lett. **29**, 679–682 (2003).
[17]G. A. Mesyats, M. I. Yalandin, K. A. Sharypov, V. G. Shpak, and S. A. Shunailov, IEEE Trans. Plasma Sci. **36**, 2497–2504 (2008).
[18]A. G. Abramov, E. I. Asinovskii, and L. M. Vasilyak, Sov. J. Quantum Electron. **13**, 1203–1206 (1983).
[19]I. V. Adamovich, W. R. Lempert, M. Nishihara, J. W. Rich, and Y. G. Utkin, J. Propul. Power **24**, 1198–1214 (2008).
[20]I. V. Adamovich, M. Nishihara, I. Choi, M. Uddi, and W. R. Lempert, Phys. Plasmas **16**, 113505 (2009).
[21]S. M. Starikovskaia, E. N. Kukaev, A. Y. Kuksin, M. M. Nudnova, and A. Y. Starikovskii, Combust. Flame **139**, 177–187 (2004).
[22]S. V. Pancheshnyi, S. M. Starikovskaia, and A. Y. Starikovskii, J. Phys. D: Appl. Phys. **32**, 2219–2227 (1999).
[23]B. T. Yee, B. R. Weatherford, E. V. Barnat, and J. E. Foster, J. Phys. D: Appl. Phys. **46**, 505204 (2013).
[24]E. V. Barnat and K. Frederickson, Plasma Sources Sci. Technol. **19**, 055015 (2010).
[25]Q. Wang, D. J. Economou, and V. M. Donnelly, J. Appl. Phys. **100**, 023301 (2006).
[26]D. X. Liu, P. Bruggeman, F. Iza, M. Z. Rong, and M. G. Kong, Plasma Sources Sci. Technol. **19**, 025018 (2010).
[27]W. P. Winn, J. Appl. Phys. **38**, 783–790 (1967).
[28]E. V. Barnat and V. I. Kolobov, Appl. Phys. Lett. **102**, 034104 (2013).
[29]E. V. Barnat, IEEE Trans. Plasma Sci. **39**, 2608–2609 (2011).
[30]N. Y. Babaeva and M. J. Kushner, Plasma Sources Sci. Technol. **18**, 035010 (2009).
[31]A. A. Kulikovsky, J. Phys. D: Appl. Phys. **33**, 1514 (2000).